Atomic-scale probing of heterointerface phonon bridges in nitride semiconductor

Yue-Hui Li[a,b], Rui-Shi Qi[a,b], Ruo-Chen Shi[a,b], Jian-Nan Hu[c], Zhe-Tong Liu[b], Yuan-Wei Sun[a,b], Ming-Qiang Li[b], Ning Li[b], Can-Li Song[c], Lai Wang[d], Zhi-Biao Hao[d], Yi Luo[d], Qi-Kun Xue[c,e,f], Xu-Cun Ma[c], and Peng Gao[a,b,g,h,1]

[a]International Center for Quantum Materials, School of Physics, Peking University, Beijing 100871, China; [b]Electron Microscopy Laboratory, School of Physics, Peking University, Beijing 100871, China; [c]State Key Laboratory of Low-Dimensional Quantum Physics, Department of Physics, Tsinghua University, Beijing 100084, China; [d]Beijing National Research Center for Information Science and Technology, Department of Electronic Engineering, Tsinghua University, Beijing 100084, China; [e]Beijing Academy of Quantum Information Sciences, Beijing 100193, China; [f]Department of Physics, Southern University of Science and Technology, Shenzhen 518055, China; [g]Interdisciplinary Institute of Light-Element Quantum Materials and Research Center for Light-Element Advanced Materials, Peking University, Beijing 100871, China; and [h]Collaborative Innovation Centre of Quantum Matter, Beijing 100871, China

Interface phonon modes that are generated by several atomic layers at the heterointerface play a major role in the interface thermal conductance for nanoscale high-power devices such as nitride-based high-electron-mobility transistors and light-emitting diodes. Here we measure the local phonon spectra across AlN/Si and AlN/Al interfaces using atomically resolved vibrational electron energy-loss spectroscopy in a scanning transmission electron microscope. At the AlN/Si interface, we observe various interface phonon modes, of which the extended and localized modes act as bridges to connect the bulk AlN modes and bulk Si modes and are expected to boost the phonon transport, thus substantially contributing to interface thermal conductance. In comparison, no such phonon bridge is observed at the AlN/Al interface, for which partially extended modes dominate the interface thermal conductivity. This work provides valuable insights into understanding the interfacial thermal transport in nitride semiconductors and useful guidance for thermal management via interface engineering.

nitride semiconductor | interface phonons | STEM-EELS

Rapid developments of various modern information technologies such as big data transmission, cloud computing, artificial intelligence technology, and the internet of things have put forward higher requirements on network transmission speed and capacity, demanding higher-power and higher-speed electronic devices (1, 2) such as nitride-based high-electron-mobility transistors (3). Thermal management in such devices becomes crucial as the high output power density results in a strong Joule self-heating effect, which increases the channel temperature and severely degrades device performance (4, 5). Solutions for thermal management include searching for high-thermal-conductivity materials (6, 7) and increasing interface thermal conductance (ITC) via interface engineering (8–10). The latter approach becomes increasingly important when the size of the device approaches nanoscale as the ITC dominates the device's thermal resistance (11, 12). However, it is challenging to obtain precise knowledge of ITC due to the atomic size and the buried nature of heterointerfaces. The common methods to characterize thermal conductivity, including the time-domain thermoreflectance (13), the frequency-domain thermoreflectance (14), the 3-ω method (15), and coherent optical thermometry (16), suffer from a poor spatial resolution that is insufficient to measure thermal properties at the nanoscale.

In fact, the thermal properties of semiconductor and insulator interfaces are largely governed by the interface phonons, and interface phonons also dominate the ITC of metal/semiconductor interfaces because electron–phonon coupling has little effect on the ITC of metal/semiconductor interfaces and can be ignored (17, 18). Previous calculations indicate that the interface can bridge the phonons with different energies and thus boost the inelastic phonon transport (19). Recent methods such as modal analysis were used to correlate the interface phonons

with interfacial heat flow (20–23). Specifically, the interface phonon modes can be classified into four classes: extended modes (EMs), partially extended modes (PEMs), isolated modes (IMs), and localized modes (LMs), based on how the vibrational energy is distributed in space (22). The atomic vibrations are delocalized into both sides of the interface for EMs and are localized on one side for PEMs. IMs are not present at the interface, while LMs are highly localized at the atomically thin interface.

Of the four modes, EMs and LMs can act as phonon bridges to increase the chances of phonons crossing the interface by elastic/inelastic scattering, while PEMs and IMs only have a small transmission probability for phonon transport. The delocalized EMs exhibit strong correlation between phonons of both sides, thus effectively serving as phonon bridges to support the phonons of one side to cross the interface to the other side via both elastic and inelastic scattering (22, 24). LMs, arising from the few atomic layers at the interface, exhibit extremely strong correlation with phonon modes of both sides, thus effectively serving as phonon bridges to facilitate frequency up and down conversion. As a result, the phonons in one side dump their energy to LMs at the interface region and then transfer it to the phonons in the other side (22, 25). This process can

Significance

As high-power devices approach nanoscale, interface thermal conductance (ITC) becomes a bottleneck to govern the device performance, which is dominated by the interface phonons. In order to gain insights into engineering ITC, here we measure the local phonons across AlN/Si and AlN/Al interfaces by using atomically resolved vibrational electron energy-loss spectroscopy. We find that the dominant types of interface phonons for ITC are very different in these two systems and demonstrate the ability to correlate the measured interface phonons with ITC at atomic scale. Our study reveals the underlying mechanism of ITC and provides useful insights for thermal management in these practically important semiconductors.

PHYSICS

bridge the phonons with significantly different energies through inelastic scattering. Indeed, LMs usually have the highest contribution to the ITC on a per-mode basis (19, 22, 26, 27). Very recently, the localized modes for MoS_2/WSe_2 (28), Ge/Si (29), $SrTiO_3/CaTiO_3$ superlattices (30), and cubic-BN/diamond system (31) have been experimentally observed. At a Ge/Si interface, calculations suggested a small number of LMs make substantial contributions to ITC, acting as bridges to connect the bulk modes of two sides, while IMs hardly contribute to ITC (25). However, the dominant type of interface phonons for ITC is likely different in different material systems depending on the interface bonding. It is thus useful to experimentally study nanoscale phonon behaviors at various interfaces and correlate them to thermal conductance across the interface.

In this work, we study interface phonons at the AlN/Si and AlN/Al heterointerfaces. Due to the wide bandgap, high-breakdown electric field, and high carrier mobility, the III-V nitride semiconductors such as GaN, AlN, and their ternary compounds are considered promising in the next-generation high-power and high-frequency electronic devices (32), which, however, requires excellent thermal conductivity, especially high ITC (33). For these nitride heterostructures, it remains largely unknown what types of interface phonons exist, not to mention how they impact the ITC and which one dominates. By using vibrational electron energy-loss spectroscopy (EELS) in a scanning transmission electron microscope (STEM), which has the ability to measure the phonon spectra (34–37) at atomic scale (28, 29, 38–42), we probe the interface phonons to gain insights into interface thermal properties.

We observe multiple types of interface phonons at an AlN/Si interface and find that EMs that connect the bulk AlN phonon modes and bulk Si phonon modes, and LMs that promote a transverse acoustic (TA) mode of Si to penetrate into the AlN layer, act as bridges to mainly contribute to ITC. However, no such bridging effect is observed across the AlN/Al interface where PEMs dominate, while EMs and LMs only take up a small proportion in the total modes. The AlN/Si interface is therefore expected to have a much higher ITC than the AlN/Al interface since EMs and LMs contribute many times larger than PEMs to the ITC according to molecular dynamics (MD) simulations. Our results unveil the very different interface phonon modes at the heterointerfaces of AlN/Si and AlN/Al and find they have very different contributions to the ITC, providing insights into understanding and engineering the interface thermal properties.

Results and Discussion

The AlN (0001) film was grown on an Si (111) substrate. To exclude the long-range dipole scattering and significantly improve the relative contribution of highly localized impact scattering signal, the direct beam is moved off the optical axis and outside the EELS aperture (*SI Appendix*, Fig. S1), which enables us to obtain the local vibrational information (42) (*SI Appendix*, Figs. S2 and S3). Fig. 1*A* displays the atomic-resolution high-angle annular dark field (HAADF) image of AlN/Si interface along the $[11\bar{2}0]$ direction of AlN and the $[1\bar{1}0]$ direction of Si, wherein the Si and Al atoms form covalent Si–Al bonds and would significantly influence the vibrational properties near the interface.

Fig. 1*B* displays the EEL spectral mapping across the AlN/Si interface. The line profile of EEL spectra is provided in *SI Appendix*, Fig. S4. Considering scattering wave vectors are predominately in the plane of the specimen perpendicular to the electron beam (43, 44), the phonon dispersions, the projected in-plane Brillouin zones, and in-plane components of the phonon density of states (PDOS) of Si and AlN calculated from the MD are displayed in Fig. 1*C*. In the bulk regions, the
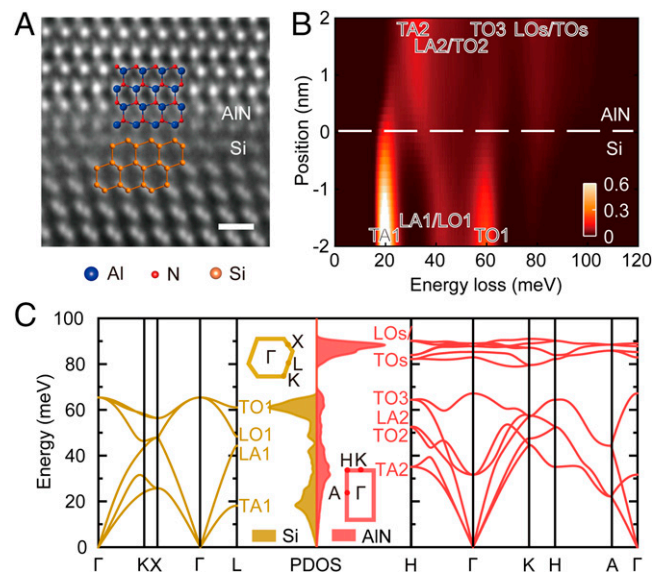

Fig. 1. Atomic structure and phonon spectra of the AlN/Si interface. (*A*) Atomic HAADF images and structure of the AlN/Si interface. (Scale bar, 0.5 nm.) (*B*) Mapping of phonon EEL spectra across the AlN/Si interface. (*C*) Phonon dispersions, projected Brillouin zones, and in-plane component of PPDOS of Si and AlN.

characteristic vibrational peaks in Fig. 1*B* can be assigned based on the calculations and refs. 45–47. For the Si bulk phonon spectrum, three peaks at 19.8 meV, 43.8 meV, and 59.0 meV are assigned to Si-TA1 mode, longitudinal acoustic/longitudinal optical (Si-LA1/LO1) mode, and transverse optical (Si-TO1) mode, respectively. For the AlN bulk phonon spectrum, four peaks at 31.5 meV, 45.0 meV, 63.2 meV, and 80.0 meV are AlN-TA2 mode, AlN-LA2/TO2 mode, AlN-TO3 mode, and AlN-LOs/TOs mode, respectively. It should be noted that AlN-LOs/TOs mode is composed of several optical phonon branches with close frequencies. We find that Si-TA1 mode penetrates into AlN layer, Si-LA1/LO1 mode connects to AlN-TA2 mode, and Si-TO1 mode also connects to AlN-TO3 mode at the interface forming bridges across the interface. AlN-LOs/TOs modes penetrate into Si layer but decays rapidly within ~1 nm.

In order to gain insights into the physical origin of different spectral features at the interface, MD simulation was performed using the Large-scale Atomic/Molecular Massively Parallel Simulator (LAMMPS) package (48, 49) with the Stillinger-Weber potential (50, 51). Fig. 2 *A* and *B* show the measured phonon spectra and the calculated in-plane component of projected PDOS (PPDOS) of bulk AlN, AlN/Si interface, and bulk Si. The arrows represent the energy shift of Si-TA1 mode from the Si layer to the interface and AlN-TA2 mode from the AlN layer to the interface, respectively. The experimental spectra in Fig. 2*A* show a blueshift of ~3.4 meV for Si-TA1 mode and a blueshift of ~1.5 meV for AlN-TA2 mode at the interface, which is in reasonable agreement with the simulated spectra in Fig. 2*B* with a blueshift of ~4.4 meV for Si-TA1 mode and ~1.8 meV for AlN-TA2 mode. Notably, the relative higher height of Si-TA1 and AlN-TA2 in the experimental data (Fig. 2*A*) compared to the calculation (Fig. 2*B*) derives from the Boson occupation statistics at room temperature (52). The corrected spectra by removal of the predicted statistical distortion are much closer to in-plane component of PPDOS, as shown in *SI Appendix*, Fig. S5.

To quantitatively validate these spectral features, the background-subtracted vibrational spectra were fitted using a simple Gaussian peaks fitting model. Fig. 2 *C* and *D* show the fitted peak positions and peak intensities across the AlN/Si
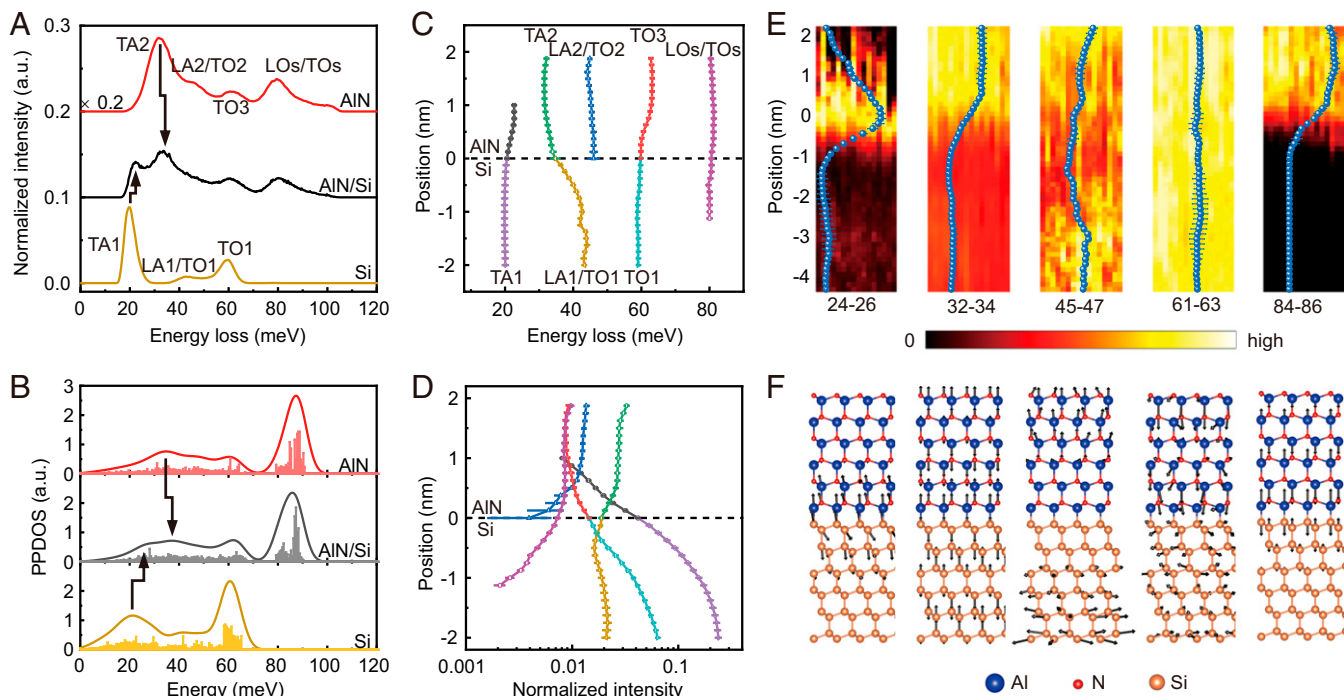
Fig. 2. Interface phonons at the AlN/Si interface. (*A*) Measured EEL spectra and (*B*) calculated in-plane component of PPDOS of bulk AlN, AlN/Si interface, and bulk Si. The arrows represent the blueshift of Si-TA1 mode and AlN-TA2 mode at the interface. (*C*) Fitted phonon peak positions across the AlN/Si interface. (*D*) Phonon peak intensities across the AlN/Si interface. The peak positions and intensities are extracted by Gaussian peaks-fitting method. (*E*) Intensity maps of different phonon modes and the corresponding intensity line profiles. (*F*) Corresponding calculated eigenvector displacements of interface phonon modes.

interface, respectively. Si-TA1 mode penetrates into the AlN layer and has a slight blueshift with intensity decreased by ~15 times within ~1 nm. Si-LA1/LO1 mode and AlN-TA2 mode have an energy shift near the interface and connect to each other to form a phonon bridge. Si-TO1 mode and AlN-TO3 mode also have a slight energy shift and connect to the other as a phonon bridge. These phonon bridges connect the phonons with significantly different energies and promote phonon transport across the interface to contribute thermal conductance (19). AlN-LA2/TO2 mode only exists in AlN layer and has a sharp intensity decrease near the interface, which contributes little to thermal conductance. AlN-LOs/TOs mode penetrates into Si layer and also makes a contribution to ITC.

Fig. 2*E* shows energy-filtered EELS maps of five typical phonon branches in Fig. 2*C*. Fig. 2*F* shows the corresponding calculated vibrational eigenvector displacements. In the intensity map of 24 to 26 meV, the vibrational intensity is localized near the interface with a peak width of ~1.5 to 2 nm, and the simulated vibrational eigenvector displacement below also displays that the vibration is localized at the interface, indicating an LM. In addition, the corresponding dispersion curves projected onto the interfacial layer appear outside of the bulk bands in *SI Appendix*, Fig. S6, which further demonstrate its localized character. The intensity maps of 32 to 34 meV and 61 to 63 meV showing strong intensities in both sides are EMs, as further confirmed by the simulated eigenvector displacements. The intensity map of 45 to 47 meV corresponds to an IM which is not present at the interface, while the intensity map of 84 to 86 meV corresponds to a PEM whose vibration mainly exists in the AlN side.

In comparison, we also measured the phonon spectra across an AlN/Al interface as an example of a typical semiconductor/metal-electrode interface. Fig. 3*A* displays the atomic-resolution HAADF image and atomic structure of the AlN/Al

interface, where the Al atoms on the Al (111) plane and the Al atoms on the AlN (0001) plane form Al–Al metallic bonds like those in bulk Al layer. Fig. 3*B* shows mapping of the background-subtracted vibrational spectra across the AlN/Al interface. Fig. 3*C* displays the phonon dispersion, the projected Brillouin zone, and corresponding in-plane component of PPDOS of Al and AlN based on the MD calculations. For the Al bulk spectrum, two peaks located at 22.8 meV and 30.6 meV are assigned to Al-TA3 and Al-LA3 modes, respectively, based on the MD calculations and ref. 46. Fig. 3*D* displays the typical EEL spectra of bulk AlN, bulk Al, and the AlN/Al interface. The line profile of EEL spectra is provided in *SI Appendix*, Fig. S7. Different from the AlN/Si interface, no distinct LMs are observed to connect the phonons with significantly different energies in two sides. The fitted peak position line profile in Fig. 3*E* shows Al-TA3 mode and Al-LA3 mode terminate at the interface with a subtle energy shift. AlN-TO3 mode just abruptly disappears at the interface, while the AlN-LOs/TOs mode penetrates into the Al layer for ~1.5 nm. The intensity maps of 22 to 24 meV, 61 to 63 meV, and 81 to 83 meV in Fig. 3*F* indicate most of these modes are PEMs, which means a very small part of phonons can cross the interface. Especially between 22 and 24 meV, although there is some overlap in PPDOS between Al and AlN, only a small part of the phonons propagates in the AlN (*SI Appendix*, Fig. S7). This can be understood by the fact that the phonon propagation depends on not only the DOS overlap but also the mode match (53). Indeed, the calculated eigenvector in *SI Appendix*, Fig. S8 shows that in this energy range the amplitude in AlN is far smaller than that in Al, which is indicative of PEM. The 38 to 40 meV is likely made up of LM and PEM, and the 29 to 31 meV corresponds to an EM.

Fig. 4 shows the calculated modal contribution to ITC (denoted by G) for each mode class at AlN/Si and AlN/Al
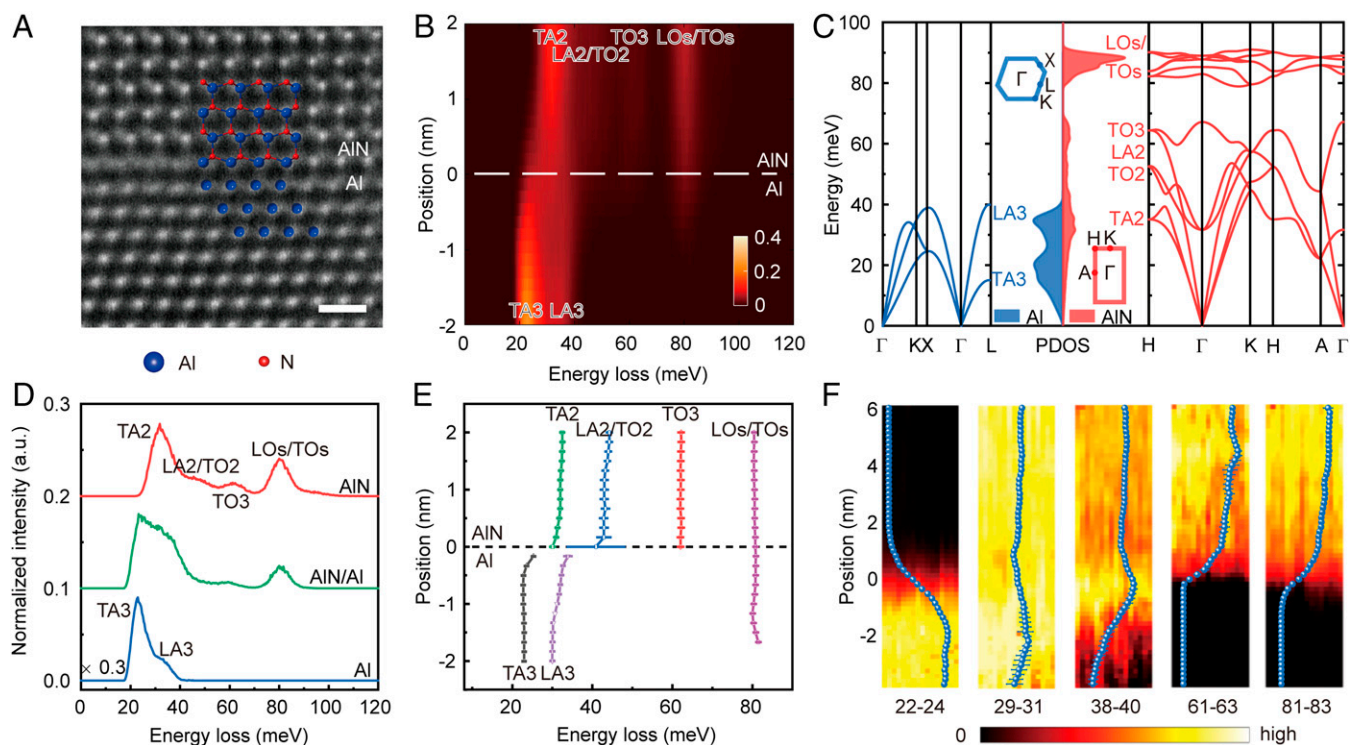
Li et al.
Atomic-scale probing of heterointerface phonon bridges in nitride semiconductor

PNAS | 3 of 6
https://doi.org/10.1073/pnas.2117027119

PHYSICS

Fig. 3. Atomic structure and interface phonons of AlN/Al. (*A*) Atomic HAADF images and structure of the AlN/Al interface. (Scale bar, 0.5 nm.) (*B*) Mapping of phonon EEL spectra at the AlN/Al interface. (*C*) Phonon dispersions, projected Brillouin zones, and in-plane component of PPDOS of Al and AlN. (*D*) EEL spectra of bulk AlN, the AlN/Al interface, and bulk Al. (*E*) Phonon peak positions across the AlN/Al interface. (*F*) Intensity maps of different phonon modes and the corresponding intensity line profiles.

interfaces. The EMs have vibration components on both sides and act as bridges for the phonons of the two sides and have more contribution to ITC on a per-mode basis (larger G/DOS) than the PEMs. In fact, the EMs comprise ~45% of total

Fig. 4. DOS and contribution to ITC for the four different classes of vibration across the AlN/Si interface and AlN/Al interface. (*Top*) The fraction of total DOS. (*Middle*) The fraction of total ITC. (*Bottom*) The contribution to ITC per mode.

DOS in AlN/Si system, but only ~22% of total DOS in AlN/Al system, which explains that the ITC of AlN/Si ($\sim 300\ \mathrm{MW \cdot m^{-2} \cdot K^{-1}}$) (54) is larger than that of AlN/Al ($\sim 117\ \mathrm{MW \cdot m^{-2} \cdot K^{-1}}$) (55). Our nonequilibrium MD simulation also obtains the same conclusion, i.e., the ITC of AlN/Si ($\sim 330\ \mathrm{MW \cdot m^{-2} \cdot K^{-1}}$) is higher than that of AlN/Al ($\sim 103\ \mathrm{MW \cdot m^{-2} \cdot K^{-1}}$). IMs contribute little to ITC because there is no vibration near the interface (22). Although both our and previous (22) results show that the LMs have the highest contribution (G/DOS) on a per-mode basis, their low population makes them contribute no more than 10% of total ITC.

Conclusion

In summary, we have directly measured the interface phonon modes of AlN/Si and AlN/Al heterointerfaces at atomic scale using STEM-EELS. We experimentally obtain and distinguish different interface phonon modes at the AlN/Si and find that the EMs and LMs can act as phonon bridges to contribute heavily to the ITC by elastic/inelastic scattering. In contrast, no obvious phonon bridge is observed in the AlN/Al system since it has low population for EMs but very high population for PEMs that contribute less to ITC. These features account for their significantly different ITC. The demonstrated ability to directly correlate the measured interface phonons with thermal transport properties at heterointerfaces on an atomic level opens new avenues for engineering the interface thermal properties for thermal management and thermoelectric devices.

Materials and Methods

Interface Fabrication. In a molecular beam epitaxy chamber, the Al/AlN sample was grown on Si(111) substrate. As with the growth procedure reported before (56), substrate nitridation for 60 s and alumination under Al flux irradiation for 900 s were performed for formation of AlN nucleation layer on
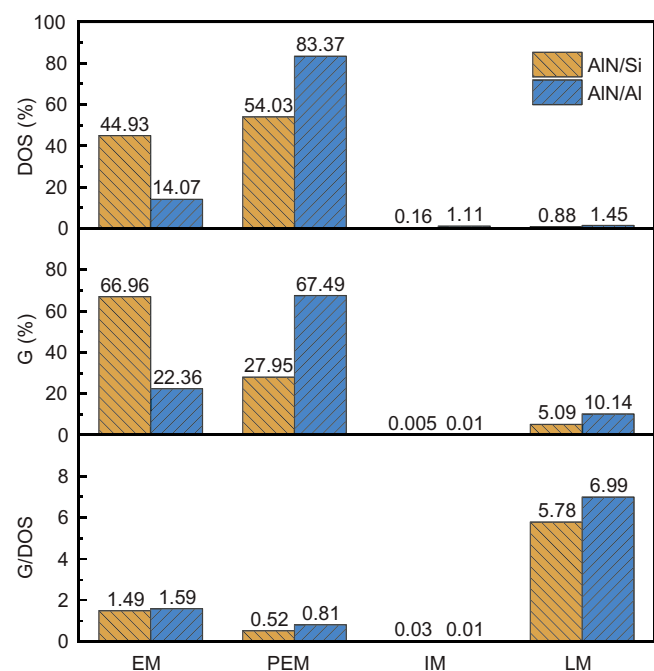
Si(111). After the growth of the AlN layer, the nitrogen source was turned off, and the substrate temperature was lowered for growth of Al metal layer. Reflection high-energy electron diffraction patterns of Al layer were kept streaky, and Kikuchi lines were observed, indicating two-dimensional growth mode and flat surface of the Al layer. Finally, AlO_x were formed on the top by natural oxidation after exposure to atmosphere for protection of the Al layer.

TEM Sample Preparation. The cross-sectional STEM specimen was prepared by conventional mechanical polishing followed by argon ion milling. The argon ion milling was carried out using the Precision Ion Polishing System (model 691; Gatan Inc.). The accelerating voltage was first set at 3.5 kV with angles $\pm$ 6° until a hole was made and then lowered to 1.0 kV with angles $\pm$ 3° until the hole was enlarged to the interface, and finally lowered to 0.1 kV for 2 min to remove the surface amorphous layer without damage. The specimen was baked at 160°C for 16 h to further remove the surface contamination layer before EELS experiments.

Experimental Setup. The vibrational spectra were acquired at a Nion U-HERMES200 electron microscope equipped with both the monochromator and the aberration corrector operated at 30 kV. The probe convergence semi-angle and the collection semiangle were both 25 mrad. The electron beam was moved off optical axis with 80 mrad for off-axis experiments to greatly reduce the contribution of the dipole scattering. Moreover, the vibrational spectra with such large convergence semiangle, collection semiangle, and off-axis angle are close to the in-plane component of localized PPDOS (42–44). The energy dispersion channel was set as 0.35 meV with 2,048 channels in total. The typical beam current was ~12 pA. The best energy resolution (full width of half maximum) was ~6.2 meV for on-axis experimental setup and ~7.5 meV for off-axis experimental setup when the beam was focused on the specimen. The spatially resolved EEL spectra in Figs. 1*B* and 3*B* were originally recorded as a spectrum image, with single exposures of 1,600 ms per pixel. The acquired spectrum images are 2 nm × 10 nm with 0.125 nm per pixel in Fig. 1*B* and 2.7 nm × 12 nm with 0.166 nm per pixel in Fig. 3*B*. The acquired EEL spectra before background subtraction are shown in *SI Appendix*, Fig. S9. The specimen thickness is measured ~30 nm near the interface by using log-ratio method (57), as shown in *SI Appendix*, Fig. S10. The HAADF image were recorded by an aberration-corrected FEI Titan Themis G2 operated at 300 kV.

EELS Data Processing. All acquired vibrational spectra were processed using the Gatan Microscopy Suite and custom-written MATLAB code. The EEL spectra were first aligned by their normalized cross-correlation. Next, the block-matching and three-dimensional filtering (BM3D) algorithm were applied to remove Gaussian noise. All spectra were then normalized to the intensity of zero-loss peak. The background arising from both the tail of ZLP and noncharacteristic phonon losses was fitted using the modified Peason-VII function (41, 58) with two fitting windows and then subtracted to obtain the vibrational signal. The Lucy–Richardson algorithm was then employed to ameliorate the broadening effect caused by finite energy resolution, taking the elastic ZLP as the point spread function. The spectra were summed along the direction parallel to the interface to obtain a line-scan data with a good signal-to-noise ratio. Then the spectra within ± 2 nm near the interface were cropped because the bridging effects are localized within ± 1 nm near the interface. The vibrational spectra were fitted using a simple Gaussian peaks-fitting model to extract the peak positions and peak intensities.

MD Simulation. The MD simulations were performed using the LAMMPS package (48) with the Stillinger–Weber potential (50, 51). The atomic plane of Si (111) and AlN (0001) are mismatched, e.g., the lattice constants are $a_{Si(111)}$ = 3.88 Å and $a_{AlN(0001)}$ = 3.15 Å experimentally. It is hard for MD simulations to simulate such mismatched interfaces since it requires a large cross-section area to fit $a_{Si(111)}$ and $a_{AlN(0001)}$. To overcome this difficulty, we can either set the average lattice constant in the directions parallel to the interface, $a_{\parallel}$ = ($a_{Si(111)}$ + $a_{AlN(0001)}$)/2, and set the lattice constant in the directions perpendicular to the interface, $a_{\perp}$, to give a zero stress in that direction (59) or change the interatomic potential of Si to be the same as AlN so that they have the same lattice constant $a_{AlN(0001)}$ (19). We choose the second method for it works better near the interface (19). The computational code, Dynaphophy, is used to extract the phonon properties from MD simulations (49).

Recently developed interface conductance modal analysis (22, 60) enables us to determine the modal contribution to ITC by substituting the modal contributions into either an equilibrium MD or nonequilibrium MD expression for ITC. The modal ITC is

$$G_n = \frac{1}{k_B A T^2} \int \langle J_n(t)J(0)\rangle dt,$$

where k_B is the Boltzmann constant, A is the cross-sectional contact area, and T is the absolute temperature. $J_n(t)$ and $J(0)$ are the mode-specific heat currents with a separation time of t. The $\langle\cdots\rangle$ brackets indicate averaging over different time origins. Based on the magnitude of the eigenvectors (22), the modes were classified into four distinct classes: extended, partially extended, isolated, and localized modes, and then we can obtain their contribution to ITC.

Phonon Modes Classification. Based on MD simulations, we can obtain the eigenvectors of the interface phonon modes. The interface phonon modes are classified into four classes, based on their vibrations with respect to the interface according to the literature (22). First, four parameters are defined to measure the magnitude of the eigenvectors in a given mode. For example, in the AlN/B (B = Si, Al) system, the parameters are defined as follows:

$$P_{i,\,tot} = \sum_{j\in entire\ system} |e_{i,j}|$$

$$P_{i,\,int} = \sum_{j\in interface\ region} |e_{i,j}|$$

$$P_{i,\,AlN} = \sum_{j\in AlN} |e_{i,j}|$$

$$P_{i,\,B} = \sum_{j\in B} |e_{i,j}|,$$

where $e_{i,j}$ represents the vibration amplitude of atom j and eigen mode i. The interface region usually contains the atoms within two unit cells from the interface plane. The four classifications are then defined as

1) extended modes: $0.001 < P_{i,int}/P_{i,tot} < 0.5$, $0.1 \le P_{i,AlN}/P_{i,B} \le 10$;
2) partially extended modes: $0.001 \le P_{i,int}/P_{i,tot} \le 0.5$, $P_{i,AlN}/P_{i,B} > 10$, or < 0.1;
3) isolated modes: other modes; and
4) localized modes: $P_{i,int}/P_{i,tot} > 0.5$.

Generally, the vibration of EMs are delocalized into both materials, the majority of the vibration of PEMs mainly exists on one side of the interface, the vibration of IMs are not present at the interface, and the majority of LMs are highly localized at the interface.

Data Availability. All study data are included in the article and/or *SI Appendix*.

1. F. Roccaforte, G. Greco, P. Fiorenza, F. Iucolano, An overview of normally-off GaN-based high electron mobility transistors. *Materials (Basel)* **12**, 1599 (2019).
2. R. Sun, J. Lai, W. Chen, B. Zhang, GaN power integration for high frequency and high efficiency power applications: A review. *IEEE Access* **8**, 15529–15542 (2020).
3. J. Zhu *et al.*, Piezotronic effect modulated flexible AlGaN/GaN high-electron-mobility transistors. *ACS Nano* **13**, 13161–13168 (2019).
4. S. Li *et al.*, High thermal conductivity in cubic boron arsenide crystals. *Science* **361**, 579–581 (2018).
5. L. Li, A. Fukui, A. Wakejima, Bonding GaN on high thermal conductivity graphite composite with adequate interfacial thermal conductance for high power electronics applications. *Appl. Phys. Lett.* **116**, 142105 (2020).
6. F. Tian *et al.*, Unusual high thermal conductivity in boron arsenide bulk crystals. *Science* **361**, 582–585 (2018).
7. J. S. Kang *et al.*, Integration of boron arsenide cooling substrates into gallium nitride devices. *Nat. Electron.* **4**, 416–423 (2021).
8. X. Qian, J. Zhou, G. Chen, Phonon-engineered extreme thermal conductivity materials. *Nat. Mater.* **20**, 1188–1202 (2021).
9. M. N. Luckyanova *et al.*, Phonon localization in heat conduction. *Sci. Adv.* **4**, eaat9460 (2018).
10. Z. Tian, K. Esfarjani, G. Chen, Enhancing phonon transmission across a Si/Ge interface by atomic roughness: First-principles study with the Green's function method. *Phys. Rev. B* **86**, 235304 (2012).
11. A. Giri, P. E. Hopkins, A review of experimental and computational advances in thermal boundary conductance and nanoscale thermal transport across solid interfaces. *Adv. Funct. Mater.* **30**, 1903857 (2020).
12. H. Bao, J. Chen, X. Gu, B. Cao, A review of simulation methods in micro/nanoscale heat conduction. *ES Energy Environ.* **1**, 16–55 (2018).

Li et al.
Atomic-scale probing of heterointerface phonon bridges in nitride semiconductor

PNAS | 5 of 6
https://doi.org/10.1073/pnas.2117027119

13. D. G. Cahill, Analysis of heat flow in layered structures for time-domain thermoreflectance. *Rev. Sci. Instrum.* **75**, 5119–5122 (2004).

14. A. J. Schmidt, R. Cheaito, M. Chiesa, A frequency-domain thermoreflectance method for the characterization of thermal properties. *Rev. Sci. Instrum.* **80**, 094901 (2009).

15. D. G. Cahill, R. O. Pohl, Thermal conductivity of amorphous solids above the plateau. *Phys. Rev. B Condens. Matter* **35**, 4067–4073 (1987).

16. D. M. Toyli, C. F. de las Casas, D. J. Christle, V. V. Dobrovitski, D. D. Awschalom, Fluorescence thermometry enhanced by the quantum coherence of single spins in diamond. *Proc. Natl. Acad. Sci. U.S.A.* **110**, 8417–8421 (2013).

17. R. E. Jones, J. C. Duda, X. W. Zhou, C. J. Kimmer, P. E. Hopkins, Investigation of size and electronic effects on Kapitza conductance with non-equilibrium molecular dynamics. *Appl. Phys. Lett.* **102**, 183119 (2013).

18. P. Singh, M. Seong, S. Sinha, Detailed consideration of the electron-phonon thermal conductance at metal-dielectric interfaces. *Appl. Phys. Lett.* **102**, 181906 (2013).

19. T. Feng, Y. Zhong, J. Shi, X. Ruan, Unexpected high inelastic phonon transport across solid-solid interface: Modal nonequilibrium molecular dynamics simulations and Landauer analysis. *Phys. Rev. B* **99**, 045301 (2019).

20. K. Sääskilahti, J. Oksanen, J. Tulkki, S. Volz, Role of anharmonic phonon scattering in the spectrally decomposed thermal conductance at planar interfaces. *Phys. Rev. B* **90**, 134312 (2014).

21. Y. Zhou, M. Hu, Full quantification of frequency-dependent interfacial thermal conductance contributed by two- and three-phonon scattering processes from nonequilibrium molecular dynamics simulations. *Phys. Rev. B* **95**, 115313 (2017).

22. K. Gordiz, A. Henry, Phonon transport at interfaces: Determining the correct modes of vibration. *J. Appl. Phys.* **119**, 015101 (2016).

23. A. J. Gabourie, Z. Fan, T. Ala-Nissila, E. Pop, Spectral decomposition of thermal conductivity: Comparing velocity decomposition methods in homogeneous molecular dynamics simulations. *Phys. Rev. B* **103**, 205421 (2021).

24. A. Rohskopf, R. Li, T. Luo, A. Henry, A computational method for studying vibrational mode dynamics. arXiv [Preprint] (2021). https://arxiv.org/abs/2108.04795 (Accessed 5 December 2021).

25. K. Gordiz, A. Henry, Phonon transport at crystalline Si/Ge interfaces: The role of interfacial modes of vibration. *Sci. Rep.* **6**, 23139 (2016).

26. C. A. Polanco et al., Design rules for interfacial thermal conductance: Building better bridges. *Phys. Rev. B* **95**, 195303 (2017).

27. A. Giri et al., Interfacial defect vibrations enhance thermal transport in amorphous multilayers with ultrahigh thermal boundary conductance. *Adv. Mater.* **30**, e1804097 (2018).

28. X. Tian et al., Capturing 3D atomic defects and phonon localization at the 2D heterostructure interface. arXiv [Preprint] (2021). https://arxiv.org/abs/2104.08978 (Accessed 24 July 2021).

29. Z. Cheng et al., Experimental observation of localized interfacial phonon modes. *Nat. Commun.* **12**, 6901 (2021).

30. E. R. Hoglund et al., Nanoscale phonon spectroscopy reveals emergent interface vibrational structure of superlattices. arXiv [Preprint] (2021). https://arxiv.org/abs/2105.10030 (Accessed 14 August 2021).

31. R. Qi et al., Measuring phonon dispersion at an interface. *Nature* **599**, 399–403 (2021).

32. U. K. Mishra, P. Parikh, Y. Wu, AlGaN/GaN HEMTs-an overview of device operation and applications. *Proc. IEEE* **90**, 1022–1031 (2002).

33. Z. Cheng, F. Mu, L. Yates, T. Suga, S. Graham, Interfacial thermal conductance across room-temperature-bonded GaN/diamond interfaces for GaN-on-diamond devices. *ACS Appl. Mater. Interfaces* **12**, 8376–8384 (2020).

34. O. L. Krivanek et al., Vibrational spectroscopy in the electron microscope. *Nature* **514**, 209–212 (2014).

35. M. J. Lagos, A. Trügler, U. Hohenester, P. E. Batson, Mapping vibrational surface and bulk modes in a single nanocube. *Nature* **543**, 529–532 (2017).

36. N. Li et al., Direct observation of highly confined phonon polaritons in suspended monolayer hexagonal boron nitride. *Nat. Mater.* **20**, 43–48 (2021).

37. S. Huang et al., Recent progress of vibrational electron energy-loss spectroscopy in scanning transmission electron microscope. *J. Vac. Sci. Technol.* **3**, 213–224 (2021).

38. K. Venkatraman, B. D. A. Levin, K. March, P. Rez, P. A. Crozier, Vibrational spectroscopy at atomic resolution with electron impact scattering. *Nat. Phys.* **15**, 1237–1241 (2019).

39. F. S. Hage, D. M. Kepaptsoglou, Q. M. Ramasse, L. J. Allen, Phonon spectroscopy at atomic resolution. *Phys. Rev. Lett.* **122**, 016103 (2019).

40. X. Yan et al., Single-defect phonons imaged by electron microscopy. *Nature* **589**, 65–69 (2021).

41. R. Qi et al., Four-dimensional vibrational spectroscopy for nanoscale mapping of phonon dispersion in BN nanotubes. *Nat. Commun.* **12**, 1179 (2021).

42. F. S. Hage, G. Radtke, D. M. Kepaptsoglou, M. Lazzeri, Q. M. Ramasse, Single-atom vibrational spectroscopy in the scanning transmission electron microscope. *Science* **367**, 1124–1127 (2020).

43. P. Rez et al., Damage-free vibrational spectroscopy of biological materials in the electron microscope. *Nat. Commun.* **7**, 10945 (2016).

44. G. Radtke et al., Polarization selectivity in vibrational electron-energy-loss spectroscopy. *Phys. Rev. Lett.* **123**, 256001 (2019).

45. L. Lindsay, D. A. Broido, T. L. Reinecke, Ab initio thermal transport in compound semiconductors. *Phys. Rev. B Condens. Matter Mater. Phys.* **87**, 165201 (2013).

46. J. M. Winey, A. Kubota, Y. M. Gupta, A thermodynamic approach to determine accurate potentials for molecular dynamics simulations: Thermoelastic response of aluminum. *Model. Simul. Mat. Sci. Eng.* **17**, 055004 (2009).

47. V. Yu. Davydov et al., Phonon dispersion and Raman scattering in hexagonal GaN and AlN. *Phys. Rev. B* **58**, 12899–12907 (1998).

48. S. Plimpton, Fast parallel algorithms for short-range molecular dynamics. *J. Comput. Phys.* **117**, 1–19 (1995).

49. A. Carreras, A. Togo, I. Tanaka, DynaPhoPy: A code for extracting phonon quasiparticles from molecular dynamics simulations. *Comput. Phys. Commun.* **221**, 221–234 (2017).

50. F. H. Stillinger, T. A. Weber, Computer simulation of local order in condensed phases of silicon. *Phys. Rev. B* **31**, 5262–5271 (1985).

51. F. F. Krause et al., Using molecular dynamics for multislice TEM simulation of thermal diffuse scattering in AlGaN. *Ultramicroscopy* **189**, 124–135 (2018).

52. P. E. Batson, M. J. Lagos, Interpretation of meV resolution phonon EELS data. *Microsc. Microanal.* **24**, 412–413 (2018).

53. B. Latour, N. Shulumba, A. J. Minnich, Ab initio study of mode-resolved phonon transmission at Si/Ge interfaces using atomistic Green's functions. *Phys. Rev. B* **96**, 104310 (2017).

54. B. E. Belkerk et al., Substrate-dependent thermal conductivity of aluminum nitride thin-films processed at low temperature. *Appl. Phys. Lett.* **105**, 221905 (2014).

55. R. L. Xu et al., Thermal conductivity of crystalline AlN and the influence of atomic-scale defects. *J. Appl. Phys.* **126**, 185105 (2019).

56. J. Hu et al., Atomically smooth and homogeneously N-polar AlN film grown on silicon by alumination of Si₃N₄. *Appl. Phys. Lett.* **102**, 141913 (2013).

57. T. Malis, S. C. Cheng, R. F. Egerton, EELS log-ratio technique for specimen-thickness measurement in the TEM. *J. Electron Microsc. Tech.* **8**, 193–200 (1988).

58. B. D. A. Levin, K. Venkatraman, D. M. Haiber, K. March, P. A. Crozier, Background modelling for quantitative analysis in vibrational EELS. *Microsc. Microanal.* **25**, 674–675 (2019).

59. E. S. Landry, A. J. H. McGaughey, Thermal boundary resistance predictions from molecular dynamics simulations and theoretical calculations. *Phys. Rev. B* **80**, 165304 (2009).

60. H. R. Seyf, K. Gordiz, F. DeAngelis, A. Henry, Using Green-Kubo modal analysis (GKMA) and interface conductance modal analysis (ICMA) to study phonon transport with molecular dynamics. *J. Appl. Phys.* **125**, 081101 (2019).